Kinematic Simulation of Fully Developed Turbulent Channel Flow

Neil R. Clark · John Christos Vassilicos

Abstract We detail a new method of generating kinematic simulation fields in a channel. We employ a new decomposition for kinematic simulation which ensures that the boundary conditions are automatically satisfied while preserving incompressibility. We impose statistics up to second order, including the Reynolds shear-stress and one-dimensional spectral densities. We observe streak-like structures kinematically similar to those observed in the laboratory, with a similar scaling with the wall-normal distance. We explain the appearance and scaling of the streak-like structures in terms of the two-dimensional spectra imposed on the fields.

1 Introduction

Normally, one calculates a turbulent flow field and its time development from the Navier-Stokes equations directly or from a filtered version of these equations, and then one calculates statistics, including correlations and turbulent flow profiles.

An alternative approach is to go from the statistics to turbulent flow fields which obey them. Examples of such approaches are the Proper Orthogonal Decomposition (POD) (see [1]) and Kinematic Simulations (see [4]). Kinematic Simulations (KS) are based on a Eulerian synthetic velocity field which is designed to obey certain

N. R. Clark
D.A.M.T.P., University of Cambridge, Centre for Mathematical Sciences,
Wilberforce Road, Cambridge CB3 0WA, UK

J. C. Vassilicos (✉)
Department of Aeronautics, Imperial College, London SW7 2BY, UK
e-mail: j.c.vassilicos@imperial.ac.uk

one-point and two-point statistics. KS is then typically used to calculate Lagrangian turbulence statistics [3].

To date, KS models have been developed for homogeneous isotropic turbulence [2–5] and for homogeneous non-isotropic turbulence, specifically strongly stratified and/or fast rotating homogeneous turbulence [6, 11]. All these KS models have produced Lagrangian statistics which compare generally well with theoretical expectations and DNS, though there is a debate concerning turbulent pair diffusion in isotropic turbulence [12, 13]. KS of homogeneous isotropic turbulenc has also been successfully used as an LES subgrid model for scalar variances [23]. However, no KS has ever been devised for non-homogeneous turbulence.

Here, we present a method of conducting a kinematic simulation for fully-developed turbulent channel flow. The problem which accompanies inhomogeneity is that of satisfying the wall boundary conditions which is not trivial as it forces a complete rewrite of the KS synthetic velocity field in terms of its basis functions and the imposition of the prescribed Eulerian statistics. Anisotropy, inhomogeneity, wall boundaries, incompressibility, mean flow profile, various energy spectra and axial mean momentum balance are all incorporated into the kinematic simulation presented here for the first time.

The reason why KS is successful in cheaply calculating relatively accurate Lagrangian turbulence statistics is that it incorporates qualitatively correct eddying, straining and streaming flow structures mainly through the imposition of incompressibility and energy spectra [2, 4]. Though not quantitatively accurate, this flow topology closely resembles what is observed in turbulent flow visualisations, and lends the Lagrangian trajectories their geometry and, in turn, accurate Lagrangian statistics [3]. Wall flows and inhomogeneous anisotropic turbulence have their own associated flow topology which our KS will need to qualitatively capture to some degree.

Slow stream-wise elongated streak structures are perhaps the most well recognised organised structures in turbulent channel flows. These structures are described kinematically as stream-wise elongated regions of negative fluctuating stream-wise velocity. Streak structures scaling with the inner length scale were first observed in the sub log-layer region of turbulent wall flows ([7, 15], see also reviews by [8, 9] and [10]). Since then streaks scaling with the outer length scale have been also observed in the log layer [14, 16, 17]. The stream-wise length of the log-layer streaks also appear to increase in proportion to distance from the wall [20]. The kinematic simulation of a fully developed turbulent channel flow presented here automatically generates elongated stream-wise structures. These slow elongated regions are not only kinematically similar to the streaks of real turbulence, but can also scale in a similar way [20]. As much of the success of kinematic simulation of homogeneous isotropic flows has been attributed to its incorporation of the appropriate flow structures it is significant that kinematic simulation reproduces such a dominant flow structure.

2 Kinematic Simulation Fields

Before describing the method to generate kinematic simulation fields in the channel we briefly review the construction of kinematic simulation fields of isotropic

homogeneous flows. In many studies the construction of the field is via a random superposition of Fourier waves [4] thus,

$$\mathbf{u}(\mathbf{x}, t) = \sum_{n=0}^{N_k} \mathbf{a_n} \cos(\mathbf{k_n}.\mathbf{x} + \omega_n t) + \mathbf{b_n} \sin(\mathbf{k_n}.\mathbf{x} + \omega_n t) \tag{1}$$

where N_k is the total number of modes included, $\mathbf{a_n}$ and $\mathbf{b_n}$ are decomposition coefficients corresponding to the wave vector $\mathbf{k_n}$, and ω_n is the unsteadiness frequency. The effects of molecular diffusion are neglected [25, 26].

The wave vectors included in the superposition,

$$\mathbf{k_n} = k_n \hat{\mathbf{k_n}} \tag{2}$$

are oriented randomly by ensuring that the unit vectors $\hat{\mathbf{k_n}}$ have a random, uniformly distributed, orientation. The magnitude of the wave vectors included in the summation can be given an arbitrary distribution. Usually they are decimated so as to reduce computational demands, while including enough modes for the convergence of the Lagrangian statistics. The authors of [27] tried arithmetic, geometrical, and linear distributions and found that the distribution

$$k_n = k_1 \left(\frac{k_{N_k}}{k_1} \right)^{(n-1)/(N_k-1)}, \tag{3}$$

where n is an integer satisfying $1 \leq n \leq N_k$, gives the fastest convergence of the statistics.

The coefficient vectors $\mathbf{a_n}$ and $\mathbf{b_n}$ are chosen randomly and independently in the plane normal to the $\mathbf{k_n}$,

$$\mathbf{a_n}.\mathbf{k_n} = \mathbf{b_n}.\mathbf{k_n} = 0. \tag{4}$$

This also ensures that the random field is incompressible.

In order to impose an energy spectrum, $E(k)$ upon the field, the magnitudes of the coefficients are chosen such that

$$|\mathbf{a_n}|^2 = |\mathbf{b_n}|^2 = 2E(k_n)\Delta k_n, \tag{5}$$

where

$$\Delta k_n = \frac{k_{n+1} - k_{n-1}}{2}. \tag{6}$$

Usually the spectrum used is of the inertial range form,

$$E(k) = C_k \epsilon^{2/3} k^{-5/3}, \tag{7}$$

but departures from this scaling have also been studied, partly for intermittency corrections but also to try to gauge the importance of the energy spectrum scaling to the Lagrangian statistics in kinematic simulation.

The time dependence of the field is incorporated through the unsteadiness frequency ω_n. This is often equated with the eddy turnover time of the nth mode, $\omega_n = \lambda \sqrt{k_n^3 E(k_n)}$. A wide range of values of the constant λ have been studied, from near-frozen fields to extremely unsteady fields.

In the following sections we proceed to detail the more involved method of generating kinematic simulation fields in the channel. The method of construction

of kinematic simulation fields, though simple in the isotropic homogeneous case, is complicated by the presence of walls because the boundary conditions are difficult to satisfy in the Fourier basis. Therefore, in the presence of walls we no longer use a basis of pure independent Fourier modes. As we show in this paper, it is possible to find a complete set of basis fields which are individually incompressible so that our fields would be incompressible by construction and such that each basis field meets the boundary conditions at the wall, so the field would not only be incompressible but also satisfy the boundary conditions at the wall by construction.

Our random fields should also have a prescribed energy spectrum just as in the isotropic homogeneous case, but this time we shall be concerned with the one-dimensional spectral density, for simplicity and also because of the greater volume of experimental data and theoretical background existing for this statistic. In the case of the three-dimensional channel, we will see that after constraining the one-dimensional spectral density there is freedom enough to also specify the Reynolds shear-stress profile. We shall also impart a mean flow profile of our choosing upon the fields.

However the specification of a given energy spectrum is now no longer straightforward. As we are no longer dealing with pure Fourier waves, but some arbitrary basis, we can no longer treat each mode separately. In this arbitrary basis, if we calculate the coefficients of a random field with a prescribed energy spectrum, we find that the coefficients of the included modes become coupled.

In the following two sections we describe the manner in which kinematic simulation fields can be constructed in the specific cases of two and three-dimensional channels (pipe flows can in principle be treated in an analogous way). We show how an appropriate basis can be constructed and how energy spectra can be imposed on the fields. We also find that the imposed energy spectra are no longer arbitrary; there turn out to be mathematical constraints on the energy spectra that an incompressible field can support in the presence of walls. In the three-dimensional channel we describe how to impose a Reynolds shear-stress profile (i.e. the ensemble mean of the product of stream-wise and wall-normal components of Eulerian velocity) and the mathematical constraints it must satisfy. The mean flow profile and the Reynolds shear-stress in a turbulent wall flow are directly related through the balance of mean axial momentum. These two properties are imposed in Section 4 in a form which respects this relation.

As an introduction to the method of generating kinematic simulation fields in the channel we begin by describing the method for the spatially two-dimensional channel. This serves as a useful introduction to the basic method, without the complications that an extra spatial dimension brings.

3 Kinematic Simulation in a Two-Dimensional Channel

We consider the velocity field in a, spatially two-dimensional, space bounded by two straight parallel walls. A Cartesian coordinate system shall be employed, with the x and y axes parallel and normal to the wall respectively. The fields we shall consider will be periodic in the wall-parallel direction, with a periodic length which we shall call L_x. The half-width of the channel is labelled L_y. The wall-parallel direction shall be referred to as stream-wise. We shall work solely with dimensionless variables

composed of physical quantities scaled with an appropriate parameter. The non-dimensional Eulerian velocity field $\mathbf{u}(x, y)$ is scaled with the friction velocity,[1] u_τ. The non-dimensional Cartesian coordinates x and y are scaled with $L_x/2\pi$ and L_y respectively. We shall take the origin of our coordinate system to be in the centre of the channel such that the walls are located at $y = \pm 1$.

Our aim is to generate random Eulerian fields which satisfy the following constraints:

- the field must vanish at the walls:

$$\mathbf{u}(x, \pm 1) = \mathbf{0}. \tag{8}$$

- the field must be incompressible:

$$\nabla.\mathbf{u}(x, y) = 0. \tag{9}$$

- the field must have prescribed first and second order statistics.

We begin by finding an appropriate way to compose our fields. As the fields are periodic in the stream-wise direction it is simplest to compose them from Fourier waves in this coordinate and write the fields as,

$$\mathbf{u}(x, y) = \sum_k (f_k(y), g_k(y)) \, e^{ikx}, \tag{10}$$

where $f_k(y)$ and $g_k(y)$ are arbitrary complex valued scalar functions of the wall normal coordinate which only have to satisfy the reality condition $f_{-k}(y) = f_k^*(y)$, and $g_{-k}(y) = g_k^*(y)$, and k is the dimensionless stream-wise wavenumber scaled with the stream-wise periodic length L_x.

The divergenceless condition (Eq. 9) removes a degree of freedom and relates $f_k(y)$ and $g_k(y)$ through,

$$ikf_k(y) + \frac{dg_k(y)}{dy} = 0. \tag{11}$$

So these functions can be written parametrically in terms of a single scalar stream function $q(y, k)$ of the wall-normal coordinate thus,

$$f_k(y) = -\frac{d\,q(y, k)}{dy},$$

$$g_k(y) = ik\,q(y, k), \tag{12}$$

where $q(y, k)$ is an arbitrary scalar complex valued function of the wall-normal coordinate which satisfies the reality condition

$$q(y, -k) = q^*(y, k). \tag{13}$$

We can then expand our incompressible fields thus,

$$\mathbf{u}(x, y) = \sum_k \chi(y, k)e^{ikx}, \tag{14}$$

---

[1]The friction velocity, u_τ, is the appropriate velocity scale in the near-wall region of turbulent wall flows, and is defined in terms of the total stress at the wall,τ, thus, $u_\tau \equiv \sqrt{\tau_w/\rho}$.

where the vector coefficients are,

$$\chi(y, k) = \left(-\frac{dq(y, k)}{dy}, ikq(y, k) \right).$$ (15)

The no-slip and impermeability boundary conditions at the wall ultimately impose the following boundary conditions on the scalar wave function $q(y, k)$,

$$q(\pm 1, k) = 0,$$

$$\left[\frac{\partial q(y, k)}{\partial y} \right]_{y=\pm 1} = 0.$$ (16)

Thus we find an appropriate basis for the incompressible fields which meet our boundary conditions.

Now that we have a basis from which to build Eulerian fields which are incompressible and meet the boundary conditions by construction we would like to impose a particular spectral density.

The cross-power spectral density per unit stream-wise wave number $\Phi_{ij}(k, y)$ is defined such that,

$$\int_0^\infty \Phi_{ij}(k, y)dk = \overline{u_i u_j}(y),$$ (17)

where the over-line signifies the ensemble average. This is strictly defined as the Fourier transform of the correlation tensor,

$$\Phi_{ij}(k, y) = \int_0^\infty \overline{u_i(x, y)u_j(x + \gamma, y)}e^{ik\gamma} d\gamma.$$ (18)

In the case of channel flow this varies with distance from the wall and so we have included an explicit dependence on the wall-normal coordinate in the arguments.

This dimensionless form is related to the spectral density $\Phi'_{ij}(y', k')$ simply through the scaling,

$$\Phi'_{ij}(y', k') = \frac{L_x}{2\pi}u_\tau^2\Phi_{ij}(y, k),$$ (19)

where k' is the wavenumber, and y' is the wall-normal coordinate.

We wish to constrain the diagonal elements of the spectral density tensor, so we express them in terms of the decomposition derived above (Eq. 14),

$$\Phi_{xx}(y, k) = \frac{1}{\pi}\int e^{-ik\gamma}\overline{u_x(x, y)u_x(x + \gamma, y)}d\gamma = \left| \frac{\partial q(y, k)}{\partial y} \right|^2,$$

$$\Phi_{yy}(y, k) = \frac{1}{\pi}\int e^{-ik\gamma}\overline{u_y(x, y)u_y(x + \gamma, y)}d\gamma = k^2|iq(y, k)|^2,$$ (20)

We regard $\Phi_{xx}(y, k)$ and $\Phi_{yy}(y, k)$ as known functions, as our aim is to make them inputs into the model.

The equations for the stream-wise and wall-normal spectral densities are coupled by the complex valued wave function, $q(y, k)$. But we notice that both the equations

depend only on the magnitude of $q(y, k)$, so we introduce the complex phases $\alpha_1(y, k)$, and $\alpha_2(y, k)$ and write

$$\frac{\partial q(y, k)}{\partial y} = \sqrt{\Phi_{xx}(y, k)}e^{i\alpha_1(y,k)},$$

$$ikq(y, k) = \sqrt{\Phi_{yy}(y, k)}e^{i\alpha_2(y,k)}, \tag{21}$$

by taking the square-root of Eq. 20. $\alpha_1(y, k)$ and $\alpha_2(y, k)$ must be real as we require that the squared magnitude of the right hand side of the above equation be the input spectral densities. When we eliminate $q(y, k)$ from these two equations we are left with a complex equation in the two phases. Here we write the real and imaginary parts of that equation,

$$k\sqrt{\Phi_{xx}(y, k)}\cos(\alpha_1(y, k){-}\alpha_2(y, k)) = \frac{d\sqrt{\Phi_{yy}(y, k)}}{dy},$$

$$k\sqrt{\Phi_{xx}(y, k)}\sin(\alpha_1(y, k){-}\alpha_2(y, k)) = \sqrt{\Phi_{yy}(y, k)}\frac{d\alpha_2(y, k)}{dy}. \tag{22}$$

By solving these two equations, the two unknown phases $\alpha_1(k, y)$ and $\alpha_2(k, y)$ can easily be determined.

In fact we only need to solve for $\alpha_2(k, y)$,

$$\sqrt{\Phi_{yy}(y, k)}\frac{d\alpha_2(y, k)}{dy} = \pm\sqrt{\left(k\sqrt{\Phi_{xx}(y, k)}\right)^2 - \left(\frac{d\sqrt{\Phi_{yy}(y, k)}}{dy}\right)^2}, \tag{23}$$

because when this is integrated to obtain the complex phase $\alpha_2(k, y)$ in the interval $-1 \leq y \leq 1$ for a given k then the right hand side of Eq. 21 is known. For particular choices of the spectral density these integrals can be performed analytically, but generally they will need to be calculated numerically.

Once the phases have been calculated $q(y, k)$ is known, and therefore the field $\mathbf{u}(x, y)$ is known through Eqs. 14 and 15.

In integrating the differential equation for the phase $\alpha_2(k, y)$ an arbitrary constant is introduced for every wavenumber k, and there is an arbitrary sign in Eq. 23. Randomness is introduced into the fields by making the constants of integration, and the signs in Eq. 23 random variables.

We see from the differential relation for the phase $\alpha_2(k, y)$ (Eq. 23) that unless,

$$k^2\Phi_{xx}(y, k) \geq \left(\frac{d\sqrt{\Phi_{yy}(y, k)}}{dy}\right)^2, \tag{24}$$

the complex phase $\alpha_2(y, k)$ itself becomes complex, but it must be real for the field to have the input spectral densities, as mentioned earlier. Equation 24 amounts to a mutual constraint on the possible form of the input spectral densities. This arises because of the incompressibility condition and manifests itself in this way through the coupling of the components of the basis fields. Any spectrum we may wish to impose on the field must obey this constraint, and in fact only these spectra can be supported by incompressible flow in a two-dimensional channel.

We may also write the Reynolds shear-stress $R_{12}(y) = \overline{u_1 u_2}$ in terms of our field expansion,

$$R_{12}(y) = \sum_k \left(\frac{\partial q(y, k)}{\partial y} \right) (ikq(y, k))^* \tag{25}$$

which, using the definition of the phases (Eq. 21) we may write as,

$$R_{12}(y) = \sum_k \sqrt{\Phi_{xx}(k, y)} \sqrt{\Phi_{yy}(k, y)} e^{i(\alpha_1(k, y) - \alpha_2(k, y))}. \tag{26}$$

Now as this is only a function of the spectra and the phases $\alpha_1(y)$ and $\alpha_2(y)$, and the phases are determined completely by the spectra, then the Reynolds shear-stress is a function of the spectra only. Hence we only have the freedom to choose the two spectra, and the Reynolds shear-stress is fixed in terms of them.

In the next section we will construct kinematic simulation fields in a three-dimensional channel. In which case the greater freedom given by the extra dimension affords us the ability to choose not only the diagonal elements of the spectral density tensor, but also the Reynolds shear-stress profile.

4 Kinematic Simulation Fields in a Three-Dimensional Channel

In this section we will describe how an appropriate basis for kinematic simulation in the channel is constructed, how the spectra are constrained, and also how a Reynolds shear-stress profile is imposed. We will go on to describe how particular mean flow profiles, spectra and Reynolds shear-stress profiles are chosen to be imposed upon a field.

We will create incompressible fields in a three dimensional channel with a half-width L_y. The fields shall meet the no-slip and impermeability boundary conditions at the wall and will be periodic in the stream-wise and cross-stream directions as the field will be constructed to be homogeneous in those coordinates. As in the two-dimensional case, the Cartesian coordinate system is natural. We put the origin in the centre of the channel and we shall identify points within by (x', y', z') or equivalently with the indices (x'_1, x'_2, x'_3), corresponding to the directions (*stream-wise, wall-normal, cross-stream*), see Fig. 1. The mean flow is in the x' direction, and the walls are identified by $y' = \pm L_y$. The periodic length of the fields in the stream-wise and cross-stream directions are L_x, and L_z respectively. The velocity field is denoted $\mathbf{U}'(x', y', z') = \overline{\mathbf{U}}'(y) + \mathbf{u}'(x', y', z')$, where $\overline{\mathbf{U}}'$ is the mean velocity field, and $\mathbf{u}'$ is the fluctuation field. In the kinematic simulation fields the means are taken over the homogeneous coordinates. The mean velocity field is a function of the inhomogeneous coordinate y' only.

Next we define the dimensionless variables. First, the dimensionless spatial coordinates are scaled with their associated periodic length,

$$\frac{x}{2\pi} = \frac{x'}{L_x}, \qquad y = \frac{y'}{L_y}, \qquad \frac{z}{2\pi} = \frac{z'}{L_z}. \tag{27}$$
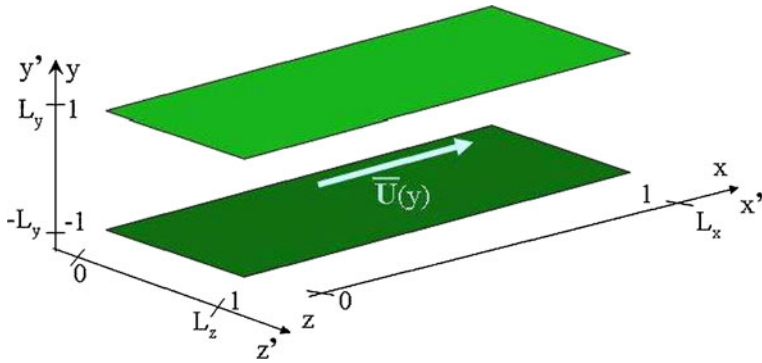
Fig. 1 Schematic of the periodic lengths of the three dimensional channel. The mean flow is in the x-direction. The flow is periodic in the two homogeneous coordinates, namely the stream-wise (period L_x) and cross-stream coordinates (period L_z). The dimensionless wall-normal coordinate y has the value -1 on the *bottom wall* and 1 on the *top wall*. L_y is the channel half width

The dimensionless velocity fields are scaled with a velocity which is labelled by u_τ in anticipation of later setting it equal to the friction velocity. The dimensionless mean-flow field is given by

$$\overline{\mathbf{U}}(y) = \frac{\overline{\mathbf{U}}'(y')}{u_\tau} \tag{28}$$

We require the velocity field to be divergenceless and to meet the no-slip and impermeability boundary conditions at the walls, so the mean and fluctuation fields must satisfy the same conditions individually. Later we will consider the mean fields, but initially we will turn our attention to the fluctuation fields. The problem we will solve in this section is to find a method of generating random Eulerian fluctuation fields in the three dimensional channel which are divergenceless,

$$\nabla . \mathbf{u}(x, y, z) = 0, \tag{29}$$

meet the no-slip and impermeability boundary conditions at the wall,

$$\mathbf{u}(x, \pm 1, z) = \mathbf{0}, \tag{30}$$

and have a prescribed spectral density. As we did in the previous section, before tackling the problem of prescribing the statistics it is first necessary to generate an appropriate basis in which to expand the fluctuation fields.

The divergence operator can be writen in terms of a dimensionless opperator thus,

$$
\begin{aligned}
\nabla' &= \left(\frac{d}{dx'}, \frac{d}{dy'}, \frac{d}{dz'} \right) \\
&= \left(\frac{2\pi}{L_x} \frac{d}{dx}, \frac{1}{L_y} \frac{d}{dy}, \frac{2\pi}{L_z} \frac{d}{dz} \right) \\
&= \left(\frac{2\pi}{L_x}, \frac{1}{L_y}, \frac{2\pi}{L_z} \right) \nabla.
\end{aligned}
\tag{31}
$$

Hence for every dimensionless field $\mathbf{u}(x, y, z)$ there exists an equivalent field,

$$\mathbf{u}'(x', y', z') = u_\tau \begin{pmatrix} C_1 \\ C_2 \\ C_3 \end{pmatrix} \mathbf{u}(x, y, z), \tag{32}$$

which has the same divergence, where the dimensionless constants C_i are in the ratio $C_1 : C_2 : C_3 = \frac{L_x}{2\pi} : L_y : \frac{L_z}{2\pi}$. We look for a basis of divergenceless fields in the dimensionless coordinates and the equivalent physical fields are given by Eq. 32.

Dimensionless variables will be used for the rest of the section and their relation to their physical equivalents indicated wherever necessary.

The first step in generating kinematic simulation fields is to generate an appropriate basis in which to decompose them. The fields are periodic in the streamwise and wall-normal directions so it is natural to employ Fourier modes in those coordinates—also, as we are considering the fluctuation field, we require the field to have a mean value of zero. Hence we shall only require the non-zero modes in the Fourier expansion. We employ two sets of radial basis vectors $\chi_{k,m}^\pm(y)$, and Fourier expand the fields thus:

$$\mathbf{u}(x, y, z) = \sum_{\substack{k=-K_{\max} \\ m=-M_{\max}}}^{\substack{k=K_{\max} \\ m=M_{\max}}} \left(\chi_{k,m}^+(y) + \chi_{k,m}^-(y) \right) e^{ikx+imz}. \tag{33}$$

Where $K_{\max}$ and $M_{\max}$ are the upper limits of the included wave-numbers, and the dimensionless wavenumbers are defined in terms of their physical counterparts k' and m' thus,

$$k' L_x = 2\pi k, \qquad m' L_z = 2\pi m. \tag{34}$$

In the same way as Leonard and Wray [21] we ensure the fields are divergence-less by generating them from the curl of a vector field thus:

$$\chi_{km}^\pm(y)e^{ikx+imz} = \nabla \times \begin{pmatrix} q_{km}^\pm(y) \\ \pm i q_{km}^\pm(y) \\ 0 \end{pmatrix} e^{ikx+imz} \tag{35}$$

$$= \begin{pmatrix} \pm m\, q_{km}^\pm(y) \\ im\, q_{km}^\pm(y) \\ \mp k\, q_{km}^\pm - \frac{d q_{km}^\pm(y)}{dy} \end{pmatrix} e^{ikx+imz}, \tag{36}$$

where $q_{km}^\pm(y)$ are arbitrary functions of y which are effectively stream-functions. The no-slip and impermeability boundary conditions at the walls ($y = \pm 1$) place the following boundary conditions on $q_{km}^\pm(y)$,

$$q_{km}^\pm(\pm 1) = 0$$

$$\left[\frac{d}{dy} \left(q_{km}^+(y) + q_{km}^-(y) \right) \right]_{y=\pm 1} = 0. \tag{37}$$

We shall return to the boundary conditions upon the stream-functions later.

The conjugate symmetry,

$$q^{\pm}_{-k-m} = \left(q^{\mp}_{km}\right)^*, \tag{38}$$

is a necessary and sufficient condition to ensure the reality of the fields.

The completeness of our fields is apparent in that the first and second components are the sum and difference of two arbitrary functions respectively, while the third is fixed by the incompressibility condition.

4.1 Imposing spectra in the three-dimensional channel

We first generate an expression for the one dimensional stream-wise spectra in terms of our field expansion (Eq. 36). We write the correlation of velocity components separated by a stream-wise distance, γ', as:

$$
\begin{aligned}
R'_{ij}(y', \gamma') &= \overline{u'_i(x', y', z')u'_i(x', y', z'} \\
&= u_\tau^2 \overline{u_i(x, y, z)u_j^*(x, y, z)} \\
&= u_\tau^2 R_{ij}(y, \gamma)
\end{aligned}
\tag{39}
$$

where $\gamma'/L_x = \gamma/2\pi$.

We can use Eqs. 32 and 33 to express $R_{ij}(y, \gamma)$ in terms of our basis. We approximate the ensemble average to the average taken over the homogeneous coordinates. Upon taking the mean over the homogeneous coordinates x, and z our expression becomes,

$$
\begin{aligned}
R_{ij}(y, \gamma) &= \sum_{k,m} C_i C_j \left(\chi^+_{km,i}(y) + \chi^-_{km,i}(y)\right) \\
&\quad \left(\chi^+_{km,j}(y) + \chi^-_{km,j}(y)\right)^* e^{-ik\gamma}.
\end{aligned}
\tag{40}
$$

As we shall be interested in the diagonal elements, we set $i = j$. The spectral densities, $\Phi_{ii}(y, k)$, can then be expressed in terms of our field decomposition thus,

$$
\begin{aligned}
\Phi_{ii}(y, k) &= C_i^2 \sum_{m=-M_{max}}^{m=M_{max}} \left|\chi^+_{km,i}(y) + \chi^-_{km,i}(y)\right|^2 \\
&= \sum_{m=-M_{max}}^{m=M_{max}} \phi_{ii}(y, k, m),
\end{aligned}
\tag{41}
$$

where $\phi_i(y, k, m)$ are the two dimensional spectra, and are related to our field expansion thus,

$$C_i^2 \left|\chi^+_{km,i}(y) + \chi^-_{km,i}(y)\right|^2 = \phi_{ii}(y, k, m). \tag{42}$$

Note that because of the symmetry of the reality condition,

$$\Phi_{ii}(y, k) = \Phi_{ii}(y, -k). \tag{43}$$

We relate these dimensionless spectra to, $\Phi'_{ii}(y', k')$, thus:

$$
\begin{aligned}
\Phi'_{ii}(y', k') &= \int_0^{L_x} \overline{u'_i(x', y', z')u'_i(x', y', z')}e^{ik'\gamma'}\,d\gamma' \\
&= \frac{L_x}{2\pi}u_\tau^2 \int_0^1 \overline{u_i(x, y, z)u_j^*(x+\gamma, y, z)}e^{ik\gamma}\,d\gamma \\
&= \frac{L_x}{2\pi}u_\tau^2 \Phi_{ii}(k, y).
\end{aligned}
$$

(44)

When imposing the spectra of [28] we shall input $\Phi'_{ii}(k'h')$, where h' is the physical distance from the nearest wall and is related to $y\prime$ by,

$$
h' = L_y - |y'|.
$$

(45)

We shall also use the dimensionless form of this variable defined as,

$$
h = \frac{h'}{L_y} = 1 - |y|.
$$

(46)

The analysis of [28] applies to a spectrum which depends only on $k'h'$, which is related to the spectra thus,

$$
\Phi'_{ii}(k'h') = h'\Phi'_{ii}(k', h'),
$$

(47)

so we can relate our dimensionless spectrum to the above form via,

$$
\Phi_{ii}(k, y) = 2\pi \frac{L_y}{L_x}h\frac{\Phi'_{ii}(k'h')}{u_\tau^2}.
$$

(48)

We can take the results of [28] for $\Phi'_{ii}(k'h')$, and relate it to $\Phi_{ii}(k, y)$ for which we have an expression in terms of our field expansion.

Now, with the dimensions accounted for we return to our relation of the two-dimensional spectra to our field expansion (Eq. 42). We can take our input one-dimensional spectrum and distribute it over the cross-stream modes thus:

$$
\Phi_{ii}(y, k) = \sum_m \phi_{ii}(y, k, m).
$$

(49)

Section 7.4 contains a discussion of the various ways we may perform this. For now we take the $\phi_{ii}(y, k, m)$ to be known functions. The question we address here is how we can specify the field components $\chi_{km,i}^{\pm}(y)$ such that the field has the desired $\phi_{ii}(y, k, m)$.

We substitute our basis (Eq. 36) to write out each component of Eq. 42,

$$
\left|C_1 m\left(Q_{km}^-(y)\right)\right|^2 = \phi_{11}(y, k, m)
$$

$$
\left|C_2 im(Q_{km}^+(y)\right|^2 = \phi_{22}(y, k, m)
$$

$$
\left|-kC_3(Q_{km}^-(y)) - C_3\frac{d}{dy}(Q_{km}^+(y))\right|^2 = \phi_{33}(y, k, m).
$$

(50)

where

$$
Q_{km}^{\pm}(y) = q_{km}^+(y) \pm q_{km}^-.
$$

(51)

We now take the square root of these equations and introduce the complex phases $\alpha_i(y, k, m)$ to obtain,

$$mQ_{km}^-(y) = \frac{\sqrt{\phi_{11}(y, k, m)}}{C_1} e^{i\alpha_1(y,k,m)}$$

$$imQ_{km}^+(y) = \frac{\sqrt{\phi_{22}(y, k, m)}}{C_2} e^{i\alpha_2(y,k,m)}$$

$$-kQ_{km}^-(y) - \frac{d}{dy}Q_{km}^+(y) = \frac{\sqrt{\phi_{33}(y, k, m)}}{C_3} e^{i\alpha_3(y,k,m)}. \tag{52}$$

At this point we take account of the boundary conditions (Eq. 37), which derive from the vanishing of the field at the wall. Expressed in terms of $Q_{km}^\pm(y)$, we can see from the three equations above that the velocity field vanishes at $y = \pm 1$, if:

$$Q_{km}^\pm(\pm 1) = 0$$

$$\left[\frac{d}{dy}Q_{km}^+(y)\right]_{y=\pm 1} = 0. \tag{53}$$

We take account of this by first introducing the functions $n_i(y)$ which contain the near-wall behaviour of the spectra, then making the substitution,

$$\sqrt{\phi_{11}(y, k, m)} = n_1(y)\sqrt{\varphi_{11}(y, k, m)}$$

$$\sqrt{\phi_{22}(y, k, m)} = n_2(y)\sqrt{\varphi_{22}(y, k, m)}$$

$$\sqrt{\phi_3(y, k, m)} = n_3(y)\sqrt{\varphi_{33}(y, k, m)}, \tag{54}$$

where $\varphi_{ii}(y, k, m)$ are functions which are equal to the spectra beyond a distance from the wall which shall correspond to the viscous layer. In conjunction with this we make the substitution,

$$Q_{km}^-(y) = n_1(y)\mathcal{Q}_{km}^-(y)$$

$$Q_{km}^+(y) = n_2(y)\mathcal{Q}_{km}^+(y), \tag{55}$$

where $\mathcal{Q}_{km}^\pm(y)$, are functions which are equal to $Q_{km}^\pm(y)$ with the viscous layer behaviour factored out. The functions $n_i(y)$ also ensure that the boundary conditions are satisfied by obeying,

$$n_i(\pm 1) = 0$$

$$\left[\frac{d}{dy}n_2(y)\right]_{y=\pm 1} = 0. \tag{56}$$

These conditions are met if, to leading order at the wall,

$$n_1(h) \propto h$$

$$n_2(h) \propto h^2$$

$$n_3(h) \propto h \tag{57}$$

This is consistent with the well known fact that the intensities, to leading order at the wall go as,

$$\overline{u_1^2(h)} \propto h^2$$

$$\overline{u_2^2(h)} \propto h^4$$

$$\overline{u_3^2(h)} \propto h^2. \tag{58}$$

We choose the $n_i(y)$ to have the value of approximately unity and to vanish at the walls over a distance corresponding to the thickness of the viscous layer. The particular way these functions vanish at the walls determines the behaviour of the spectra as the wall is approached, and the satisfaction of the boundary conditions. The form of function that we use is,

$$n_1(y) = \left(1 - e^{-\frac{1-y}{\sigma_1}}\right)\left(1 - e^{-\frac{1+y}{\sigma_1}}\right)$$

$$n_2(y) = \left(1 - e^{-\left(\frac{1-y}{\sigma_2}\right)^2}\right)\left(1 - e^{-\left(\frac{1+y}{\sigma_2}\right)^2}\right)$$

$$n_3(y) = \left(1 - e^{-\frac{1-y}{\sigma_3}}\right)\left(1 - e^{-\frac{1+y}{\sigma_3}}\right), \tag{59}$$

Where σ_i is a constant which determines the scale over which $n_i(y)$ tends to zero at the walls.

If we make the substitutions (Eqs. 54 and 55) into our equation for the spectra in terms of our field expansion (Eq. 52) we obtain the equations:

$$m\mathcal{Q}_{km}^-(y) = \frac{\sqrt{\varphi_{11}(y, k, m)}}{C_1} e^{i\alpha_1(y,k,m)}$$

$$im\mathcal{Q}_{km}^+(y) = \frac{\sqrt{\varphi_{22}(y, k, m)}}{C_2} e^{i\alpha_2(y,k,m)}$$

$$-k\mathcal{Q}_{km}^-(y) - \frac{n_2(y)}{n_1(y)}\frac{d}{dy}\mathcal{Q}_{km}^+(y) - \frac{\mathcal{Q}_{km}^+(y)}{n_1(y)}\frac{d}{dy}n_2(y)$$

$$= \frac{n_3(y)}{n_1(y)}\frac{\sqrt{\varphi_{33}(y, k, m)}}{C_3} e^{i\alpha_3(y,k,m)}. \tag{60}$$

(Note that our choice of $n_i(y)$, is such that both $n_2(y)/n_1(y)$ and $\frac{1}{n_1(y)}\frac{d}{dy}n_2(y)$ are well behaved as the wall is approached.) Now we substitute the first two of these equations into the third and eliminate $\alpha_3'(y, k, m)$ from this to obtain a differential relation for the phase $\alpha_2'(y, k, m)$,

$$\frac{n_2(y)\sqrt{\varphi_{22}(y)}}{C_2}\frac{d}{dy}\alpha_2'(y) = -\frac{kn_1(y)\sqrt{\varphi_{11}(y)}}{C_1} Sin(\alpha_1'(y))$$

$$\pm \sqrt{\frac{n_3^2(y)m^2\varphi_{33}(y)}{C_2^2} - A(y)^2}, \tag{61}$$

where for succinctness we have omitted the k and m arguments in φ_{ii}, and α'_i, and we have defined,

$$\alpha'_2(y, k, m) = \alpha_2(y, k, m) - \frac{\pi}{2}$$

$$\alpha'_1(y, k, m) = \alpha_1(y, k, m) - \alpha'_2(y, k, m)$$

$$\alpha'_3(y, k, m) = \alpha_3(y, k, m) - \alpha'_2(y, k, m)$$

and

$$A(y) = \frac{1}{C_2} \frac{d}{dy} \left(n_2(y) \sqrt{\varphi_{22}(y)} \right) + \frac{n_1(y) k \sqrt{\varphi_{11}(y)}}{C_2} Cos(\alpha'_1(y)). \tag{62}$$

We shall show in the next section that $Sin(\alpha'_1(y, k, m))$ is directly related to the Reynolds shear stress. Because the shear-stress is an input to our model $Sin(\alpha'_1(y, k, m))$ is a known function, and this fixes $\alpha'_1(y, k, m)$ up to an ambiguity in sign which we choose randomly. Then with $\alpha'_1(y, k, m)$ fixed we can integrate Eq. 61 to obtain $\alpha'_2(y, k, m)$. With these phases calculated the values of the functions $Q^{\pm}_{km}(y)$ are known from Eqs. 52 and 55. Hence the velocity field is known from Eqs. 36 and 51.

The phases $\alpha_i(y, k, m)$ must be real if the field is to have the properties of our choosing. We see that upon integrating Eq. 61 that $\alpha_2(y, k, m)$ is real only if,

$$\varphi_{33}(y) \geq \left(\frac{C_2}{n_3(y)m} A(y) \right)^2 \tag{63}$$

This constitutes a minimum constraint on the cross-stream spectrum which derives from the constraint of incompressibility. Any $\phi_{33}(y, k, m)$ that we choose to impose must meet this constraint.

We note that the differential equation for the phase $\alpha'_2(y, k, m)$ (Eq. 61) has a factor of $n_2(y)$ on the l.h.s., which means that the r.h.s must vanish at the walls at least as fast as h^2, to avoid any divergences.

The main source of randomness in the kinematic simulation fields comes from the choice of the constant of integration upon integrating Eq. 61. We label the constant of integration of $\alpha'_2(y, k, m)$, as $K(k, m)$, which we allow to be a random variable, uniformly distributed between the values of $-\pi$ and π. When included explicitly this constant appears in our field expansion thus,

$$\boldsymbol{u}(x, y, z) = \sum_{\substack{k=-K_{max} \\ m=-M_{max}}}^{\substack{k=K_{max} \\ m=M_{max}}} \left(\boldsymbol{\chi}^+_{k,m}(y) + \boldsymbol{\chi}^-_{k,m}(y) \right) e^{ikx+imz+iK(k,m)}. \tag{64}$$

Before each pair of trajectories is integrated a new set of $K(k, m)$ is randomly generated, so that each pair of particles is released into a different realisation of the kinematic simulation field.

We next describe how we constrain the Reynolds shear-stress by specifying $\alpha'_1(y, k, m)$.

4.2 Constraining the Reynolds shear stress

By setting $i = 1$, $j = 2$, and $\gamma = 0$ in Eq. 40 we generate an expression for the Reynolds shear stress in terms of our field expansion which we can write in terms of $Q_{km}^{\pm}(y)$ thus,

$$R_{12}(y) = \sum_{\substack{k=-K_{\max} \\ m=-M_{\max}}}^{\substack{k=K_{\max} \\ m=M_{\max}}} \left(C_1 m Q_{km}^-(y)\right)\left(C_2 im Q_{km}^+(y)\right)^*. \tag{65}$$

The conjugate symmetry condition on $q_{km}^{\pm}(y)$, in terms of the $Q_{km}^{\pm}(y)$, becomes,

$$Q_{-k-m}^{\pm}(y) = \pm Q_{km}^{\pm *}. \tag{66}$$

Writing this in terms of the spectra (Eq. 52), and using this we add the modes $(k, m) + (-k, -m)$ in Eq. 65 to obtain,

$$\mathcal{R}_{12}(y) = \sum_{\substack{k=1 \\ m=-M_{\max}}}^{\substack{k=K_{\max} \\ m=M_{\max}}} 2\sqrt{\varphi_{11}(y, k, m)}\sqrt{\varphi_{22}(y, k, m)} \quad Sin\left(\alpha_1'(y, k, m)\right). \tag{67}$$

Where we have factored out the near-wall behaviour of $R_{12}(y)$ in a similar way to the previous section, by making the substitution,

$$\mathcal{R}_{12}(y) = n_1(y)n_2(y)R_{12}(y) \tag{68}$$

We see that there is a maximum possible magnitude of Reynolds shear-stress, which is given by

$$\mathcal{R}_{12,max}(y) = \sum_{\substack{k=1 \\ m=-M_{\max}}}^{\substack{k=K_{\max} \\ m=M_{\max}}} 2\sqrt{\varphi_{11}(y, k, m)}\sqrt{\varphi_{22}(y, k, m)}. \tag{69}$$

If we choose to input the Reynolds shear-stress, $\mathcal{R}_{12,input}(y)$, say then we set $Sin(\alpha_1'(y))$, such that,

$$Sin\left(\alpha_1'(y)\right) = \frac{\mathcal{R}_{12,input}(y)}{\mathcal{R}_{12,max}} \tag{70}$$

then the Reynolds shear-stress of the fields will be equal to $\mathcal{R}_{12,input}(y)$ as required. This is not the most general way to achieve this however we we use it here for simplicity.

Having fixed $Sin(\alpha_1'(y, k, m))$, then, $Cos(\alpha_1'(y, k, m))$, is fixed up to a sign ambiguity. We are free to choose the sign of this function as it does not affect the relevant field statistics. We may however consider one constraint on our choice of this sign which arises from the incompressibility constraint (Eq. 63). Because $\mathcal{R}_{12,max}(y)$ and $\mathcal{R}_{12,input}(y)$ are both odd functions of y, therefore so is $Sin(\alpha_1'(y, k, m))$, hence $Cos(\alpha_1'(y, k, m))$ is an even function of y. Now we consider each of the terms in the incompressibility constraint (see Eqs. 62 and 63). The first term on the r.h.s. of Eq. 62 is odd in y, while the second term is even in y, so the sum results in an un-even

minimum $\phi_{33}(y, k, m)$ in Eq. 63. However if we choose the sign of $Cos(\alpha'_1(y, k, m))$ such that,

$$Cos\left(\alpha'_1(y, k, -m)\right) = -Cos\left(\alpha'_1(y, k, m)\right), \tag{71}$$

then when we sum over the cross-stream modes, the contribution to the minimum $\Phi_{33}(y, k)$, from $\phi_{33}(y, k, -m) + \phi_{33}(y, k, m)$, is even. This is preferable as we require statistical symmetry in y. We choose the signs randomly (1 and -1 being equally probable) while obeying this relation, this is the second source of randomness in our kinematic simulation fields.

We can now specify $\alpha'_1(y, k, m)$, substitute into Eq. 61, and integrate to obtain $\alpha'_2(y, k, m)$. Then from Eq. 52 we know the $Q^{\pm}_{km}(y)$, and hence from Eqs. 36 and 51 we can evaluate the velocity field.

4.3 The two-dimensional stream-wise spectra

We would like to impose one-dimensional stream-wise spectra, but as we saw in Eq. 49 we need to know how the stream-wise energy is distributed over the cross-stream modes (m), i.e. the two-dimensional spectra. We are to distribute our stream-wise energy in any way which obeys the incompressibility constraint, Eq. 63.

The simplest way of distributing our one-dimensional spectrum over the m-modes is,

$$\Phi_{ii}(y, k) = \sum_{m=-M_{\max}}^{m=Mmax} \phi_{ii}(y, k, m)$$

$$= \sum_{m=-M_{\max}}^{m=Mmax} g_i(k, m)\Phi_{ii}(y, k), \tag{72}$$

where for all k the distribution functions, $g_i(k, m)$, are normalised such that,

$$\sum_{m=-M_{\max}}^{m=Mmax} g_i(k, m) = 1. \tag{73}$$

In this case, by specifying $g_i(k, m)$ we effectively set,

$$\sqrt{\phi_{ii}(y, k)} = \sqrt{g_i(k, m)\Phi_{ii}(y, k)}. \tag{74}$$

The only constraint on our choice of $g_i(k, m)$ is that which derives from the incompressibility constraint (Eq. 63). We notice that for given stream-wise and wall-normal spectra, and stream-wise wave number k, the minimum constraint on the cross-stream spectrum is weaker for the larger cross-stream modes m. We find that, for given input spectra, it is necessary to distribute the stream-wise spectra over cross-stream modes which are large enough to satisfy the incompressibility constraint (Eq. 63).

This is not the most general way to prescribe the two-dimensional spectrum, however we choose to distribute in this way here as it is the simplest way in which to prescribe the one-dimensional spectra.

4.4 The decimation of the modes

As in homogeneous isotropic kinematic simulation we decimate our modes. In homogeneous kinematic simulation of [23], they found that the geometric distribution,

$$k_n = k_1 \left(\frac{k_\eta}{k_1} \right)^{\frac{n-1}{N_k - 1}}, \tag{75}$$

where the lowest and highest included wave-numbers are k_1 and k_η, and N_k is the total number of included modes.

We have chosen to decimate our modes in a similar way here, where the only modification is that we have discrete wave-numbers so we take the integer part of the distribution.

This distribution includes more modes where there is more stream-wise energy. The distribution of cross-stream modes which give the fastest convergence of Lagrangian statistics would depend on the form of the two-dimensional spectra.

5 Time Dependence

It is possible to introduce a general time dependence into our kinematic simulation fields by allowing the phases (Eq. 60) to become time dependent,

$$\alpha_i(y, k, m) \rightarrow \alpha_i(y, k, m, t).. \tag{76}$$

We could be free to choose the time dependence of this function as we choose, for example we could separate out the time dependence in a quite general way thus,

$$\alpha_i(y, k, m, t) = \alpha_i(y, k, m) + \Omega_i(y, k, m, t), \tag{77}$$

where $\Omega(y, k, m, t)$ is an arbitrary function of our choosing.

When computing the phases in this case it is necessary to evaluate the integral in Eq. 61 on a two-dimensional grid (y, t) as opposed to the one dimensional grid necessary for frozen fields, hence it is more computationally expensive (see Section 6). If however $\Omega_i(y, k, m, t)$ has no dependence on y, then there is no extra computational expense.

6 Numerical Implementation

The method described above for the generation of kinematic simulation fields in the channel is implemented in a computer code. The inputs to the code are as described in the following section. The code outputs the radial basis functions $Q_{km}^\pm(y)$ which uniquely define the velocity field.

We have employed a fourth-order Runga-Kutta routine with adaptive step-size control to integrate the $\alpha_2'(y, k, m)$ (see Eq. 61). From this and the imposed Reynolds shear-stress profile $\alpha_1'(y, k, m)$ is then calculated (using Eqs. 62 and 70). In this way we evaluate the functions $Q_{km}^\pm(y)$, from Eqs. 52 and 55 on a grid in y (Note that for a general non-trivial time dependent field it is necessary to calculate these phases on a two-dimensional grid in (y, t)).

The values of $Q_{km}^{\pm}(y)$, on the grid are stored and read by a code which evaluates the velocity field. The values of $Q_{km}^{\pm}(y)$ between the grid values are interpolated using a third order polynomial interpolation scheme. The grid is chosen to be fine enough to resolve the functions $Q_{km}^{\pm}(y)$. An appropriate integration scheme could then be used to integrate Lagrangian trajectories in the fields.

7 The Choice of the Imposed Parameters

We have to choose the following input properties of the kinematic simulation fields:

- The dimensions of the channel L_x, L_y, and L_z
- The length scale δ_v which represents the friction length scale and effectively defines the Reynolds number based on wall units.
- The one-dimensional spectra $\Phi_{ii}(y, k)$.
- The distribution of the spectra over the cross-stream modes, $g_i(k, m)$, or, more generally, the two-dimensional spectra $\phi_{ii}(y, k, m)$.
- The near wall behaviour of the spectra, $n_i(y)$.
- The mean-flow profile $\overline{U}(y)$, and the Reynolds shear-stress. Note that these are input in tandem as they are related through the mean momentum equation
- The number of included modes and how they are distributed.
- The time dependence.

We shall now discuss each of these individually:

7.1 The dimensions of the channel, L_x, L_y and L_z

The periodic lengths L_x and L_z should be large enough that the Lagrangian statistics are independent of them. It is a necessary condition therefore that particle, and pair, displacements are not significantly likely to be greater than the respective periodic length.

Also due to the relation between k' and k, (Eq. 34), the minimum possible wavenumber we can represent in our fields is when $k = 1$,

$$k'_{\min} = \frac{2\pi}{L_x}. \tag{78}$$

As we shall be imposing the spectra of [28] we would like this minimum wavenumber to be low enough to include all the features of these spectra in their range of applicability. This places a lower bound on our choice of L_x.

7.2 The Reynolds number

The Reynolds number is specified by choosing a value for the viscous length scale δ_v, then

$$Re_\tau = \frac{\delta_v}{L_y}. \tag{79}$$

Any physically meaningful spectra that we may impose will involve a greater range of excited length scales as the Reynolds number increases. The greater the range of

length scales the greater the number of modes shall be required in our field expansion (Eq. 36) for the convergence of the Lagrangian statistics.

7.3 The spectra

We are free to choose to input any spectra which obey the incompressibility constraint (Eq. 63). Here we impose the spectra with the theoretical form of [28], and we choose the parameters to be consistent with the data therein. These theoretical spectra are derived from overlap scaling arguments which are consistent with those used to derive the log-law of the mean flow, and Townsends attached eddy hypothesis [24].

The spectra apply in two regions of overlap of wall flows. In their argument, at a given distance from the wall, h, there are three relevant ranges of sales. The largest scales of motion scale with the 'outer' scale of the flow, Δ, which in the case of the channel is equivalent to the channel half-width. The intermediate range of scales ('inner scales') are of the order of h and consist of wavenumbers k which have a lower limit defined by,

$$k\Delta = F, \tag{80}$$

where F is a large scale characteristic constant, and a upper limit defined by,

$$k\eta = M, \tag{81}$$

where M is a universal constant, and η is the Kolmogorov length scale. Perry et al. [28] use an η which derives from an assumption that at a given distance from the wall, production and dissipation exactly balance. The smallest relevant length scales in the wall flow are the Kolmogorov scales.

The overlap between the outer and inner scales constitute the first overlap region, in which the stream-wise and cross-stream spectra have the form,

$$\frac{\Phi_{xx}(k'h')}{u_\tau^2} = \frac{A_x}{k'h'}$$

$$\frac{\Phi_{zz}(k'h')}{u_\tau^2} = \frac{A_z}{k'h'}, \tag{82}$$

where h' is the physical distance from the wall, A_x and A_z are universal constants. No such scaling is expected for these scales in the wall-normal spectrum because the argument is based on Townsends attached eddy hypothesis.

The overlap between the inner scales and the Kolmogorov scales constitutes the second overlap region where the spectra take the form,

$$\frac{\Phi_{xx}(k'h')}{u_\tau^2} = \frac{1}{\kappa^{\frac{2}{3}}} \frac{K_0}{(k'h')^{\frac{5}{3}}}$$

$$\frac{\Phi_{yy}(k'h')}{u_\tau^2} = \frac{1}{\kappa^{\frac{2}{3}}} \frac{\frac{4}{3}K_0}{(k'h')^{\frac{5}{3}}}$$

$$\frac{\Phi_{zz}(k'h')}{u_\tau^2} = \frac{1}{\kappa^{\frac{2}{3}}} \frac{\frac{4}{3}K_0}{(k'h')^{\frac{5}{3}}}. \tag{83}$$
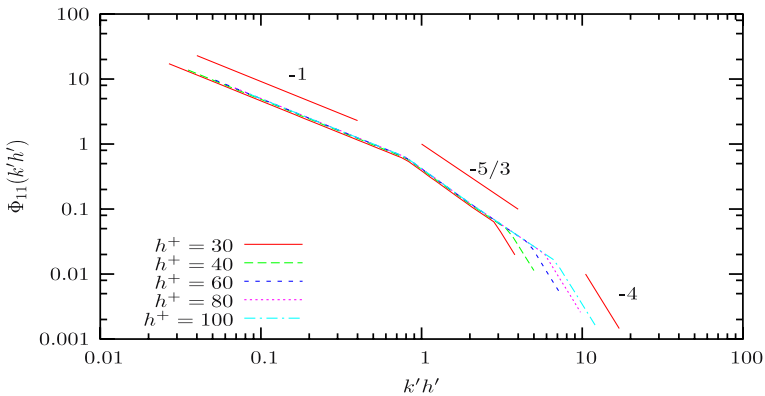
Fig. 2 The imposed stream-wise spectrum as in the spectra of Perry et al. we have a $(k'h')^{-1}$ region when $k'h' < 1$, and a $(k'h')^{-\frac{5}{3}}$ region when $k'h' > 1$. Beyond the Kolmogorov cut-off the spectra scales as $(k'h')^{-4}$. The spectrum is plotted as a function of $k'h'$ at a number of different distances from the *bottom wall* h^+

Where κ is the Karman constant. The universal constants are chosen to match the experimental measurements of the spectra by [28], and also the measured intensity profiles. We plot the input spectra in Figs. 2 and 3.

7.4 The distribution of the spectra over the cross-stream modes

As mentioned above, the only mathematical constraint upon the choice of the two-dimensional spectra is that which derives from incompressibility (Eq. 63). We have chosen to concentrate on the one-dimensional stream-wise spectra, and therefore
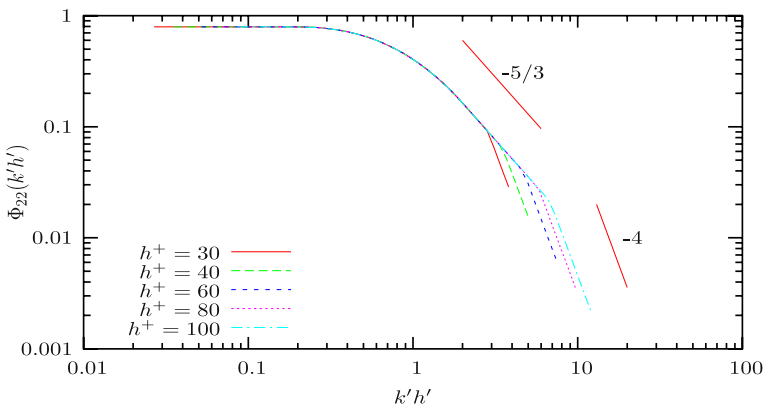

Fig. 3 The imposed stream-wise spectrum as in the spectra of Perry et al. we have a $(k'h')^{-1}$ region when $k'h' < 1$, and a $(k'h')^{-\frac{5}{3}}$ region when $k'h' > 1$. Beyond the Kolmogorov cut-off the spectra scales as $(k'h')^{-4}$. The spectrum is plotted as a function of $k'h'$ at a number of different distances from the *bottom wall* h^+

have chosen to simply distribute this over the cross-stream modes as described in Section 4.3.

Jimenez et al. [22] performed a numerical simulation of near wall turbulence and generated two-dimensional spectra. The two-dimensional spectra of [22] peaked along the line,

$$\lambda_x^+ / \lambda_z^{+\,1/3} = 13, \tag{84}$$

where λ_x^+ and λ_z^+ are the stream-wise and cross-stream wavelengths scaled with the wall unit, respectively. In which case the peak of the two-dimensional spectra always occurs at cross-stream wavelengths which are smaller than the stream-wise wavelength.

Here we continue this throughout the whole channel width,and impose a simplified distribution $g_i(k, m)$ which contains the broadest characteristics of the spectra of [22],

$$g_i(k, m) = g_{\lambda,i}\left(\lambda_x^+, \lambda_z^+\right) = \Pi_{5.5\lambda_x^{+\,1/3}, 13.5\lambda_x^{+\,1/3}}\left(\lambda_z^+\right), \tag{85}$$

where $\Pi_{a,b}(x)$ is the boxcar function, defined in terms of the Heaviside function as,

$$\Pi_{a,b}(x) = H(x - a) - H(x - b).$$

We choose this as it is the simplest distribution function which contains the most basic features of the two-dimensional spectra of [22], while also obeying the incompressibility constraint (Eq. 63).

The effect that the choice of this function has on the Lagrangian statistics and flow structures in the kinematic simulation is a matter for investigation.

7.5 The near-wall behaviour of the spectra

We define the near wall-behaviour of the spectra through the functions $n_i(y)$. These we choose to be as defined in Eq. 59. We choose the scales over which they tend to zero at the walls, σ_i, in terms of δ_v,

$$\sigma_i = 10\,\delta_v. \tag{86}$$

When this is the case the spectra tend to zero over a distance $O(10\delta_v)$, corresponding to the viscous layer, while also having the correct first-order behaviour at the walls.

7.6 The mean flow profile and the imposed Reynolds shear-stress

The mean flow profile, $\overline{U'}(y')$, is related to the Reynolds shear-stress $R_{12}'(y')$, in a turbulent wall-flow through the mean axial-momentum equation, which can be written as,

$$\frac{d}{dy'}\tau' = \frac{d}{dy'}p_w'(x'), \tag{87}$$

where $p_w'(x)$ is the mean pressure on the bottom wall of the channel, and is a function of x' only, and

$$\tau' = \rho v \frac{d}{dh'}\overline{U'}(h') - \rho\, R_{12}'(y'), \tag{88}$$

is the total stress profile, where ρ is the fluid density and v is the viscosity.

As τ' is a function of y' only, and $p'_w(y)$ is a function of x' only, then they both must be constant to satisfy Eq. 87. Then to obey the boundary conditions at the wall,

$$-\frac{d}{dx'}p'_w(x') = \frac{\tau_w}{L_y},$$

$$\tau'(y') = -\tau'_w\frac{y'}{L_y}, \tag{89}$$

where τ'_w is the total stress at the bottom wall. With this and Eq. 88 we can relate the mean flow profile and the shear-stress thus,

$$\frac{R_{12'(y')}}{u_\tau^2} = \frac{d}{dh'^+}\overline{U'}^+\left(h'^+\right) + \frac{y'}{L_y}, \tag{90}$$

where the friction velocity is given by,

$$u_\tau\sqrt{\frac{\tau'_w}{\rho}}, \tag{91}$$

and the friction length scale is defined as,

$$\delta_v = \frac{\nu}{u_\tau}. \tag{92}$$

The $^+$ indicates that the variable is scaled with the appropriate friction scale.

We now re-express this in terms of our dimensionless variables,

$$R_{12}(y) = \frac{d}{dh^+}\overline{U}^+\left(h^+\right) + y \tag{93}$$

where we use δ_v and u_τ are as defined above.

Now we choose a mean-flow profile, and then our Reynolds shear-stress shall be fixed by Eq. 93.

We impose the log-law mean flow profile over the channel width,

$$\frac{d}{dh^+}\overline{U}^+\left(h^+\right) = \frac{1}{\kappa h^+}. \tag{94}$$

However we modify this so that the mean-flow gradient vanishes smoothly, in the centre of the channel. We achieve this by multiplying by a factor which tends to zero in the centre of the channel while being close to unity over the part of the channel width which we intend to represent the log-layer. We therefor set,

$$\frac{d}{dh^+}\overline{U}^+\left(h^+\right) = \frac{1}{\kappa h^+}\left(1 - h^n\right), \tag{95}$$

where n is an exponent which is large enough to not significantly affect the log-layer profile in the part of the channel width which represents the log-layer (we have used $n = 4$).

Below the log layer we must match this profile with one which tends to zero at the wall, and which has unit gradient at the wall (universal law of the wall), i.e.,

$$\overline{U}^+(0) = 0$$

$$\left[\frac{d}{dh^+}\overline{U}^+\left(h^+\right)\right]_{h^+=0} = 1. \tag{96}$$

Fig. 4 The mean flow profile of a field with $\delta_\nu = 1/600\,L_y$, as in Eqs. 96 and 95—for the near-wall part of the function and in the rest of the channel respectively
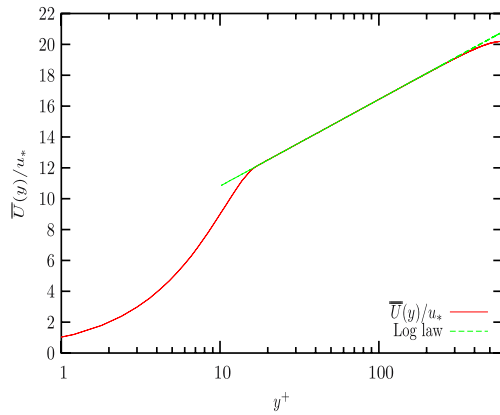

We require this sub-log-layer part of $\overline{U}^+(h^+)$ to match not only the log-layer $\overline{U}^+(h^+)$, but also that the first derivative be continuous. This is because a discontinuous first derivative in the mean flow would result in a discontinuous $R_{12}(y)$ (see Eq. 93).

For simplicity we choose to set the mean flow bellow the log region as a polynomial. In order to satisfy the law of the wall, and match the log layer and the first derivative at the boundary, we require the polynomial to be at least cubic. For simplicity we choose the cubic polynomial which matches these boundary conditions.

In this way we have a mean-flow profile which is very close to the log-layer profile over most of the channel width, while having a first derivative which continuously tends to zero in the centre of the channel, and is continuous over the whole of the channel width while vanishing at the wall obeying the law of the wall, and having a continuous first derivative across the matching boundary at $h^+ = h_m$.

Our mean-flow profile and Reynolds-shear stress profile are plotted in Figs. 4 and 5.

Fig. 5 The $R_{12}(y)$ as derived from the mean flow plotted in Fig. 4. Also plotted is the maximum possible Reynolds shear-stress for this field (see Eq. 69)— with the input spectra as plotted in Figs. 2 and 3
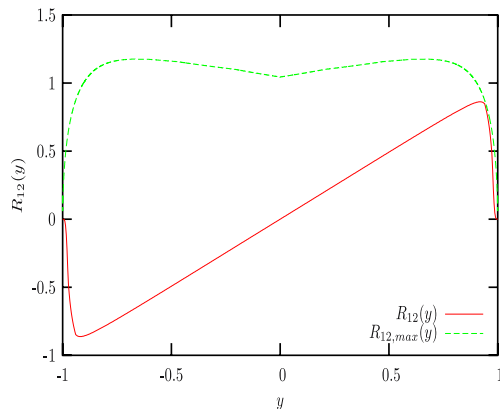
7.7 The number of modes and how they are decimated

The number of modes included in the expansion of the kinematic simulation fields needs to be large enough for convergence of the Lagrangian statistics. The decimation of modes is preferably performed in the manner which gives the fastest convergence of the Lagrangian statistics.

For the purpose of demonstration we have here decimated both the stream-wise and cross-stream modes the the manner of Eq. 75.

7.8 Time dependence

We noted in Section 5 that it is possible it impose a general time dependence on the fields. However for simplicity we use a frozen fluctuation field, which translates downstream at the bulk velocity, i.e., with our fluctuation field generated as described above we employ the kinematic simulation field,

$$\mathbf{U_{KS}}(x, y, z) = \overline{\mathbf{U}}(y) + u\,(x - U_b t, y, z)\,, \tag{97}$$

where U_b is the bulk velocity defined as,

$$U_b = \frac{1}{2L_y} \int_{-1}^{1} \overline{U}(y) dy. \tag{98}$$

Such fields will serve as a basis for comparison with fields that are given a general time dependence which depends on y, k, and m.

8 Flow Structures

Here we begin to examine the flow structure of individual realisation of kinematic simulation fields constructed as described above. We noted in the introduction the observations of slow moving elongated structures in wall flows, and the central role of flow structure in kinematic simulation. Consequently it would be significant if structures akin to the streaks in turbulent flows appeared in our kinematic simulation flows.

We plot the stream-wise component of fluctuating velocity of one typical realisation our kinematic simulation fields in a plane parallel to the bottom wall, at a distance of $20\delta_v$ from it, in Fig. 6. The white coloured regions correspond to regions where the fluctuating velocity is less than one standard deviation. We observe meandering stream-wise elongated regions similar in appearance to those seen in [14–17]. The dimensions of these streak-like structures are of the order of L_y in the stream-wise, and $\frac{1}{10}L_y$ in the cross-stream direction. We note that these streak-like structures are the largest structures in the flow and therefore must be associated with the energy residing in the lowest stream-wise wave numbers, k, where most of the stream-wise energy is concentrated. As described in Section 7.4 the stream-wise energy, at a given k, is chosen to be distributed over cross-stream wave numbers which are greater than k, consistent with [22], and also as necessitated by the
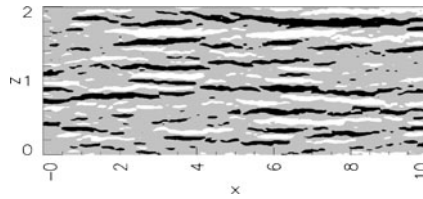
Fig. 6 The stream-wise component of fluctuating velocity plotted in a plane parallel to the walls at a distance of $20\delta_\nu$ from the *bottom wall*, from an individual realisation of a kinematic simulation field of the channel as generated above. The dimensionless coordinates (x, z) are scaled with the channel half width L_y. The *white regions* correspond to regions where $u < -\sqrt{\overline{u^2}}$, and the *black regions* correspond to regions where $u > \sqrt{\overline{u^2}}$

constraint on the spectra which derives from the incompressibility of the field (see Eq. 63). Hence most of the energy in our kinematic simulation fields is concentrated in modes with small stream-wise wave-number and larger cross-stream wave number, so perhaps it is not surprising that we observe structures which are elongated in the stream-wise direction.

We observe a lengthening of the streak-like structures with increasing distance from the bottom wall. We may also try to understand this scaling of the structures with distance from the walls, in terms of the imposed two-dimensional spectra. Most of the stream-wise energy is concentrated in the smallest k modes where the spectrum has a k^{-1} scaling. However at wavenumbers such that $kh > 1$ the spectrum falls away more rapidly having a $k^{-5/3}$ scaling. We shall now consider three spectra shown schematically in Fig. 7, in which each spectrum has kolmogorov scaling when $kh > 1$, but when $kh < 1$ the spectrum labelled (I) scales as k^{-1}, spectrum (II) is constant, and spectrum (III) scales as $k^{-5/3}$.

To understand the scaling of the streak-like structures in terms of the spectra it will be clearest to first consider spectrum (II). In this case the energy is also concentrated in the lower k modes where $kh < 1$. Upon superposing these modes they will interfere with equal weight. Therefore zero-crossings will occur on a scale determines by $kh \sim 1$, as the spectrum falls away beyond this scale. Hence we may

Fig. 7 Schematic of the three spectra
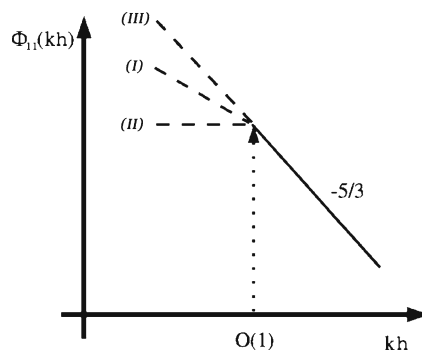
expect that the scale of stream-wise zero-crossing will increase in proportion to distance from the wall, h.

We may also apply this argument to the case of spectrum (I), however due to the k^{-1} scaling of the lower wave-numbers we may expect a weaker dependence of the streak scaling with wall-normal distance. However in the case of spectrum (III) there is no falling away of the spectrum at $kh > 1$, so we may expect that in this case the streak-like structures will not scale with distance from the wall.

In Fig. 8 we plot the stream-wise component of fluctuating velocity in three planes parallel to the walls at three heights above the bottom wall, for a field which has the spectrum (II). We can see that the streak-like structures are shorter in the plane closer to the wall. When we reproduce this plot for a field with spectrum (I) we also see a scaling of the streak-like structures with the distance from the wall, however it is weaker. Reproducing this plot for a field with spectrum (III) reveals no dependence of the streak-like structure length on distance from the wall.

We attempt to quantify this scaling in Fig. 9, where we plot the mean stream-wise extent of regions of stream-wise fluctuating velocity less than one standard deviation. This data was generated by randomly choosing positions a particular distances from the bottom wall, then using the downhill simplex method of minimisation to locate a local minimum in stream-wise velocity. If this minimum was less than the threshold than the stream-wise extent of the region was calculated and the mean taken over 3,000 samples, each in a separate realisation of the kinematic simulation field. In this figure we observe the approximately linear scaling of the lengths of the streak-like structures with distances from the wall. We observe a stronger dependence for spectrum (II) relative to spectrum (I), and no scaling for spectrum (III)—consistent with the discussion above.
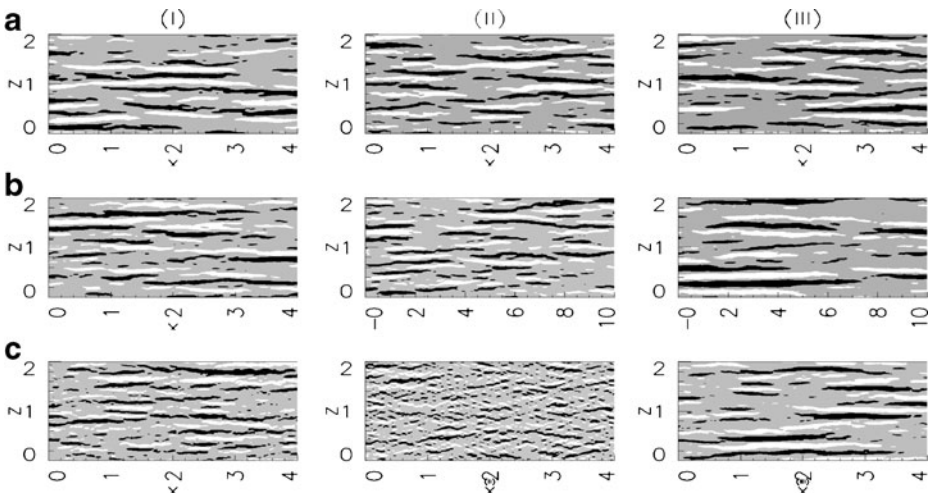

Fig. 8 The stream-wise component of fluctuating velocity in planes parallel to the *bottom wall*. The *white regions* correspond to u less than one standard deviation, the *black regions* correspond to u greater than one standard deviation. The figures in each column have spectra (I), (II), and (III) respectively. The planes in each row are at the wall normal positions **a** $h^+ = 20$, **b** $h^+ = 310$, **c** $h^+ = 600$
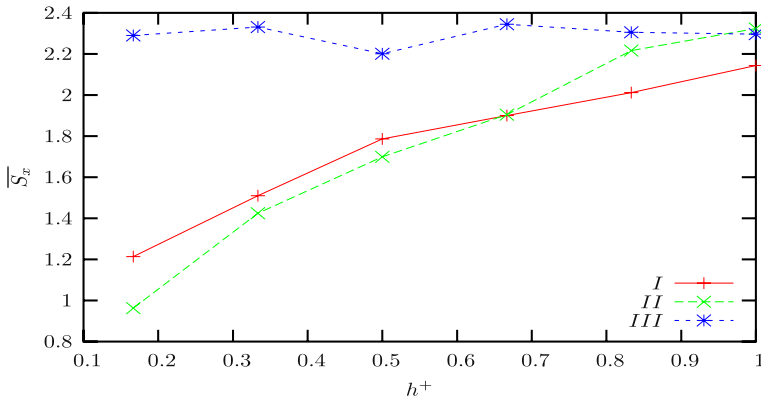
Fig. 9 The mean lengths of the stream-wise extent of regions of $u < -\sqrt{\overline{u^2}}$, at a range of distances from the wall. The *lines* represent least squared fits to functions of the form $a\, e^{b\, h}$, where a and b are the fit parameters. The exponent b has the values $0.325 \pm 6.43 \times 10^{-3}$ $0.486 \pm 5.28 \times 10^{-3}$, and $0.014 \pm 3.00 \times 10^{-3}$, for spectra *I*, *II*, and *III* respectively. We observe a stronger dependence of the lengths of the stream-wise streak-like structures as the large scale part of the spectrum becomes shallower

Fig. 10 The probability distribution of stream-wise and wall normal velocity fluctuations, $p(u, v)$, at a distance from the wall of $20\delta_v$ for a field **a** with the Reynolds stress profile as plotted in Fig. 5 **b** with zero Reynolds-shear stress but is otherwise identical. (*Darker shades* represent larger values and the *contour lines* represent values of 10^{-3}, and 10^{-4})
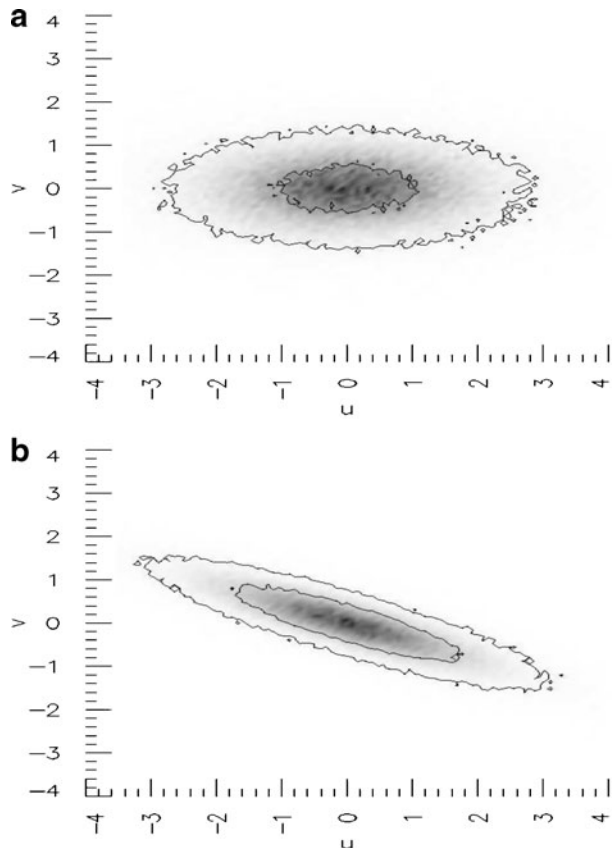
Streak structures in the near wall region of turbulent flows are associated with sweep and ejection events. In Fig. 10a we plot the two dimensional probability density function of fluctuating stream-wise and wall-normal velocity, $p(u, v)$, at a distance of $20\delta_v$ above the bottom wall. We observe that there is a preponderance of probability in the second and fourth quadrants—corresponding to 'ejection' and 'sweep' events respectively.

We may expect such a form for this probability distribution from the Reynolds sheer stress that we have input into our kinematic simulation fields. At this distance from the wall the shear-stress is large and therefore the wall-normal and stream-wise fluctuating velocities are relatively well correlated. We calculate the equivalent probability density for kinematic simulation fields which have zero shear-stress and this is shown in Fig. 10b. We observe that the probability density in this case is equally distributed throughout each quadrant.

9 Conclusion

We have demonstrated the first ever method of generating incompressible kinematic simulation fields between two plane parallel walls which meet the no-slip and impermeability boundary conditions. The boundary conditions necessitate the generation of a new basis for kinematic simulation. The method of constraining the first and second order of statistics in this new basis is more involved than previous kinematic simulation which was based on pure Fourier waves. We employ a Fourier series expansion in the homogeneous coordinates along with a radial wave function.

We derive a mathematical constraint on the one-dimensional spectra that can be imposed, which derives from the condition that the fields must be incompressible. Without the constraint of incompressibility each velocity component of the fields is independent and the choice of each of the diagonal components of the one-dimensional spectra is independent. However the condition of incompressibility removes one degree of freedom, and we find that with two of the spectra fixed, there is a minimum constraint on the third (see Eq. 63).

The effects of the imposed first and second order statistics upon the Lagrangian properties of the model is a matter for investigation. In this demonstration of the generation of kinematic simulation fields we chose to impose the log-law mean flow across most of the channel width. The log-law profile was modified in the core of the flow such that the gradient vanishes in the centre of the channel, and in the viscous layer where it was approximated to a cubic polynomial for simplicity.

We chose to impose one-dimensional stream-wise spectra based on the theoretical form of [28]. This is based on the same type of arguments used to derive the log-law of mean flow. We impose a Reynolds shear stress profile which is in accordance with the balance of mean axial momentum and the imposed mean-flow profile. We thereby impose first and second order statistics with a self-consistent theoretical basis. The method described allows the imposition of general two-dimensional spectra which obey the incompressibility constraint (Eq. 63). However for simplicity we distribute the one-dimensional spectra over the cross-stream modes in the manner of Eq. 72. We define a distribution function such that the two dimensional spectrum has the broad characteristics of the two-dimensional spectrum for the numerical simulation of [22]. We find that this allows the incompressibility constrain to be satisfied while

incorporating some of the scaling properties seen in the two-dimensional spectra of [22].

The method as demonstrated allows for a general non-trivial time dependence to be imposed on the kinematic simulation fields. For simplicity we here only generate frozen fluctuation fields which translate downstream at the bulk velocity.

We observe streak-like structures in our kinematic simulation fields in agreement, perhaps, with a recent suggestion by Chernyshenko and Baig [18]. The stream-wise elongated structures which appear in the simulation appear to be kinematically similar to the streak-structures observed in the laboratory. The structures in the model also appear to have similar dimensions and scaling properties as those in laboratory observations. We understand the appearance and scaling of these streak-like structures in terms of the imposed spectra. Future studies may reveal more of the dependence of the structure of the kinematic simulation fields upon the imposed statistics. An interesting survey of the links between structures and angle-dependent spectra in the context of homogeneous non-isotropic turbulence (e.g. stratified and/or rotating) is given by Cambon [19].

Future studies should concentrate on the Lagrangian properties of these fields. The incorporation of flow structure into the model is most significant for second and higher order Lagrangian statistics. The kinematic simulation fields as generated here could also be used as a sub-grid model for a large eddy simulation.

A directly analogous method can also be used to perform kinematic simulations of pipe flows.

The kinematic simulation of wall flows opens up a whole new line of investigation into an extremely important class of turbulent flows.

References

1. Holms, P, Lumley, J.L., Berkooz, G.: Turbulence, Coherent Structures, Dynamical Systems and Symmetry. Cambridge University Press, Cambridge (1996)
2. Fung, J.C.H., Vassilicos, J.C.: Two-particle dispersion in turbulent-like flows. Phys. Rev. E **57**(2), 1677–1690 (1998)
3. Malik, N.A., Vassilicos, J.C.: A Lagrangian model of turbulent dispersion with turbulent-like flow structure: comparison with DNS for two-particle statistics. Phys. Fluids **11**(6), 1572–1580 (1999)
4. Fung, J.C.H., Hunt, J.C.R., Malik, N.A., Perkins, R.J.: Kinematic simulation of homogeneous turbulence by unsteady random Fourier modes. J. Fluid Mech. **236**, 281–318 (1992)
5. Elliott, F.W., Majda, A.J.: Pair dispersion over an inertial range spanning many decades. Phys. Fluids **8**, 1052–1060 (1996)
6. Nicolleau, F., Yu, G., Vassilicos, J.C.: Kinematic simulation for stably stratified and rapidly rotating turbulence. Fluid Dyn. Res. **40**(1), 68–93 (2008). doi:10.1016j/fluiddyn.2006.08.011
7. Hama, F.R., Long, J.D., Hegarty, J.C.: On transition from laminar to turbulent flow. J. Appl. Phys. **28**, 388–397 (1957)
8. Panton, R.L.: Overview of the self-sustaining mechanisms of wall turbulence. Prog. Aerosp. Sci. **37**, 341–384 (2001)
9. Adrian, R.J.: Hairpin organization in wall turbulence. Phys. Fluids **19**, 041301 (2007)
10. Marusic, I., McKeon, B.J., Monkewitz, P.A., Nagib, H.M., Smits, A.J., Sreenivasan, K.R.: Wall-bounded turbulent flows at high Reynolds numbers: recent advances and key issues. Phys. Fluids **22**, 065103 (2010)
11. Cambon, C., Godeferd, F., Nicolleau, F., Vassilicos, J.C.: Turbulent diffusion in rotating turbulence with and without stable stratification. J. Fluid Mech. **499**, 231–255 (2004)

12. Thomson, D.J., Devenish, B.J.: Particle pair separation in kinematic simulations. J. Fluid Mech. **526**, 277–302 (2005)
13. Osbourne, D.R., Vassilicos, J.C., Sung, K.-S., Haigh, J.D.: Fundamentals of pair diffusion in kinematic simulations of turbulence. Phys. Rev. E **74**, 036309 (2006)
14. Ganapathisubramani, B., Hutchins, N., Hambleton, W.T., Longmire, E.K., Marusic, I.: Investigation of large-scale coherence in a turbulent boundary layer using two-point correlations. J. Fluid Mech. **524**, 57–80 (2005)
15. Kline, S.J., Reynolds, W.C., Schraub, F.A., Rundstadler, P.W.: The structure of turbulent boundary layers. J. Fluid Mech. **30**(4), 741–773 (1967)
16. Kim, K.C., Adrian, R.J.: Very large-scale motion in the outer layer. Phys. Fluids **11**, 417–422 (1999)
17. Guala, M., Hommema, S.E., Adrian, R.J.: Large-scale and very-large-scale motions in turbulent pipe flow. J. Fluid Mech. **554**, 521–542 (2006)
18. Chernyshenko, S.I., Baig, M.F.: The mechanism of streak formation in near-wall turbulence. J. Fluid Mech. **544**, 99–131 (2005)
19. Cambon, C.: Turbulence and vortex structures in rotating and stratified flows. Eur. J. Mech. B **28**, 489–510 (2001)
20. Hutchins, N., Marusic, I.: Evidence of very long meandering features in the logarithmic region of turbulent boundary layers. J. Fluid Mech. **579**, 1–28 (2007)
21. Leonard, A., Wray, A.: A new numerical method for the simulation of three-dimensional flow in a pipe. In: Eighth International Conference on Numerical Methods in Fluid Dynamics. Lecture Notes in Physics 1982, vol. 170/1982, pp. 335–342. Springer, Berlin (1982)
22. Jimenez, J., Del Alamo, J.C., Flores, O.: The large-scale dynamics of near-wall turbulence. J. Fluid Mech. **505**, 179–199 (2004)
23. Flohr, P., Vassilicos, J.C.: Scalar subgrid model with flow structure for large-eddy simulation of scalar variances. J. Fluid Mech. **407**, 315–349 (2000)
24. Townsend, A.A.: The Structure of Turbulent Shear Flow. Cambridge University Press, Cambridge (1976)
25. Sawford, B.L., Hunt, J.C.R.: Effects of turbulence structure, molecular diffusion and source size on scalar fluctuations in homogeneous turbulence. J. Fluid Mech. **165**, 373–400 (1986)
26. Borgas, M.S., Sawford, B.L.: Molecular diffusion and viscous effects on concentration statistics in grid turbulence. J. Fluid Mech. **324**, 25–54 (1996)
27. Goto, S., Osborne, D.R., Vassilicos, J.C., Haigh, J.D.: Acceleration statistics as measures of statistical persistence of streamlines in isotropic turbulence. Phys. Rev. E **71**, 015301(R) (2005)
28. Perry, A.E., Henbest, S., Chong, M.S.: A theoretical and experimental study of wall turbulence. J. Fluid Mech. **165**, 163–199 (1986)